Sensor and Simulation Notes

Note 423

2 July 1998

Design and Test of a Half Reflector IRA with Feed-Point Lens

W. Scott Bigelow

Everett G. Farr

Farr Research, Inc.

Gary D. Sower

Donald E. Ellibee

EG&G MSI

Abstract

A feed-point lens may be used to match an electrically large, oil-filled, coaxial waveguide to the feed arms of a high-voltage half reflector impulse radiating antenna (HIRA). In this note, we document the design and low-voltage test of a 1.83 m (6 ft) diameter HIRA, with a focal length-to-diameter (F/D) ratio of 1/4, and a titanium dioxide/epoxy feed-point lens with a relative dielectric constant of 7.0.

The on-boresight antenna step response is an impulse with a full-width-at-half-maximum of 70 ps. As a result of compromises in the design of the feed point, the radiated impulse was broadened somewhat, reducing the peak field. However, the measured effective aperture height of the antenna, 0.36 m, is approximately one-half the dipole moment of the reflector, as expected. Thus, the antenna performance is consistent with both theory and design.

1. Introduction

The availability of fast, single-ended, high-voltage pulsers has fueled a demand for suitable antennas to radiate the signal. A candidate antenna for this application, the Half Reflector Impulse Radiating Antenna (HIRA), was first proposed in [1], and a variation was described in [2]. The HIRA converts a plane wave in a coaxial waveguide to a spherical wave which is launched onto the conical feed arms of a (half) parabolic reflector. Upon reflection, the spherical wave is radiated as a plane wave. Normally, one would want to keep the feed point region small in order to minimize pulse distortion; but high voltages preclude that possibility. To preserve the pulse characteristics, while keeping the feed point dimensions large enough to hold off high voltages, the HIRA employs a dielectric feed-point lens to manage the conversion of the plane wave to a spherical wave.

An idealized version of a HIRA feed-point lens, employing an inhomogeneous dielectric and an array of guiding conducting sheets, was described in [3]. In [4] a practical lens, constructed from homogeneous dielectric material, was developed. The lens has a prolate spheroidal surface at the interface with the coaxial waveguide and a quartic surface of revolution at the output interface. In [5], that design was refined by linking the solution of the lens equations to the input impedance at the feed arms. Also, a figure-of-merit for the lens was defined based on maximizing the aperture integral of the electric field for the fast impulse. The analyses showed that a lens with a relative dielectric constant of 7.0 is optimal for a transition from an oil-filled coaxial waveguide to a feed point in air.

The design approach of [5] assumed a rotationally symmetric lens and conical reflector feed arm. This symmetry was computationally convenient, but its application was restricted to reflectors having a focal-length-to-diameter ratio (F/D) of 1/4, with the focus in the aperture plane of the reflector. This limitation was overcome in [6] by the introduction of offset feed-point designs that accommodate larger F/D ratios, while retaining the rotational symmetry of the feed-point lens.

On the basis of the predictions of [5], we designed a high-voltage HIRA with feed-point lens, 1.83 m (6 ft) reflector diameter, and a focal-length-to-diameter (F/D) ratio of 1/4. This note describes that antenna, its measured impedance (TDR), its radiated field on boresight, and its characteristic step response and effective aperture height. Since a high-voltage pulser was not available, these measurements were all performed with a low-voltage source. To guide the

design of this antenna and to confirm the theoretical predictions of its performance, a scale model was first constructed and tested on a ground plane in a laboratory setting. Those measurements were documented in [7], which also documented the selection and evaluation of the lens material, an epoxy paint loaded with titanium dioxide pigment. The lens material was found to have the desired relative dielectric constant of 7.0, and its breakdown strength was found adequate for pulsed high-voltage use.

The work reported in [7] demonstrated the feasibility of the full-scale high-voltage HIRA system which is the subject of this note. The system consists of the interface to the pulser, the high-voltage oil-filled coaxial feed, the feed-point lens, the radiating elements or feed arms, and the (half) parabolic reflector. The pulser interface was designed to provide a smooth impedance transition from the output of the Air Force Research Laboratory's H-5 pulser to the coaxial input of the HIRA. Since no high-voltage pulser was ultimately available for use in testing the HIRA, an interface to permit a coaxial cable connection to a low-voltage pulser was built instead.

The antenna step response is an impulse with a full-width-at-half-maximum (FWHM) on boresight of 70 ps. Compromises in the feed-point design contributed to impulse broadening and to a reduction in the peak field radiated on boresight. However, the effective aperture height, which is a measure of the area under the impulse, is 0.36 m. This is approximately one-half the dipole moment of the reflector, as expected. Thus, the performance of the antenna is consistent with both theory and design.

We now describe the full-scale HIRA system design and present measurements characterizing its performance.

2. HIRA System Design

In applying the feed-point lens design approach introduced in [5], we postulate 100 Ω HIRA driven by an oil-filled coaxial transmission line with a peak driving voltage, V_0, of 2.6 MV, and a maximum permissible electric field in the transmission line, E_{max}, of 2 MV/cm. Since the relative dielectric constant of the oil is about 2.2, the impedance of the line is about 67 Ω (100 Ω in air). Although the design calculations assume a single conical feed for the half reflector, this was replaced by a pair of equivalent 200 Ω feed cones, as indicated below.

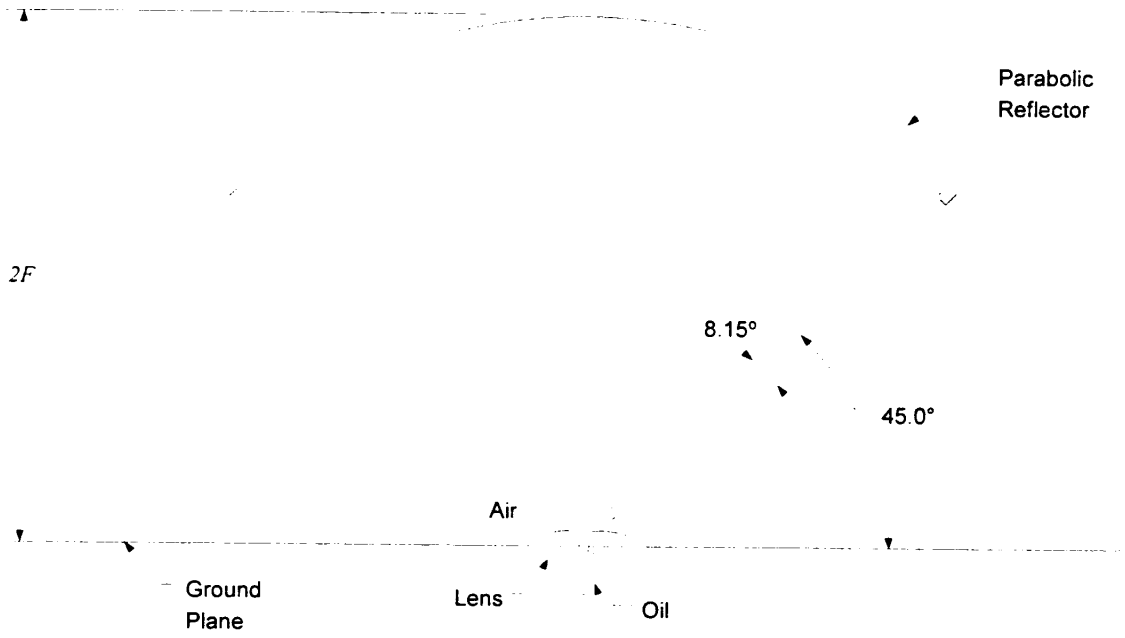

Figure 1. Concept for a two-armed HIRA with feed-point lens. In principle, the arms should intersect on the ground plane at the axis of the lens. The final design employed a somewhat simpler feed arm design.

Within the oil-filled transmission line, we have $f_g = \left(100/\sqrt{2.2}\right)/Z_0$, where $Z_0 = 376.727$ Ω is the impedance of free space. Thus, from [8, equation (4.5)], we find that an outer coaxial conductor radius of about 4 cm will keep the electric field below our postulated maximum. From [8, equation (4.3)], the corresponding inner conductor radius is 0.75 cm. Since the relative dielectric constant of the lens material is known to be 7.0, only one additional parameter needs to be specified in order to determine the feed-point lens design. That parameter is the radius of the lens at its output on the ground plane of the half reflector. We selected a radius of 12 cm as adequate to keep the field strength sufficiently low in the space between the emerging center conductor and the ground plane, about 0.3 MV/cm.

The lens equations are solved as described in [5]. with reference to the parameters identified in the following diagram. The coordinate system origin is at the intersection of the ground plane with the z-axis, which is an axis of rotational symmetry. The oil-lens interface is a

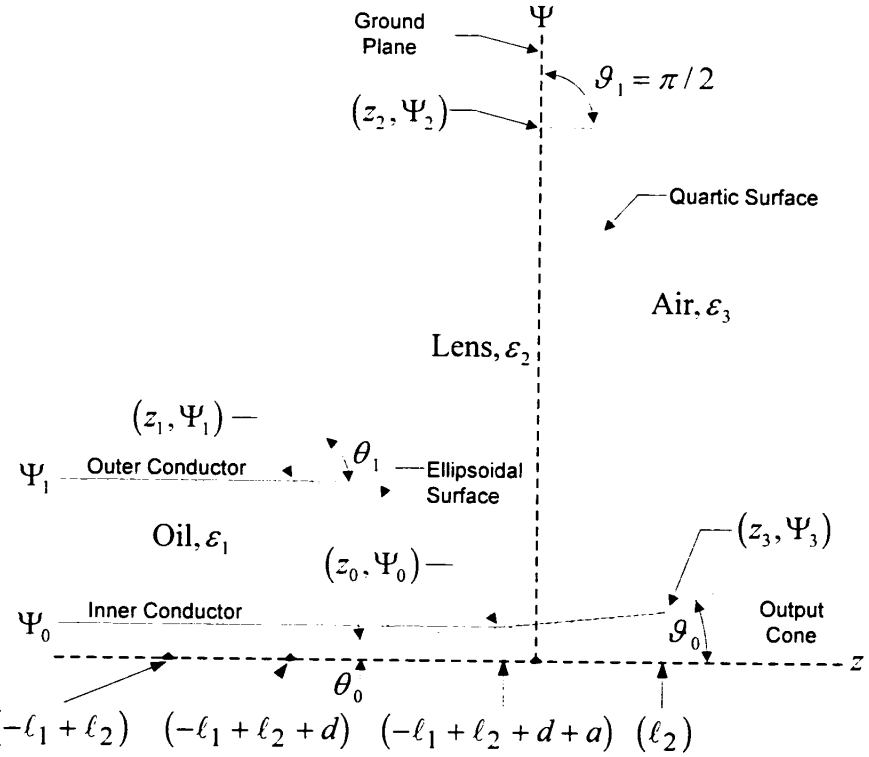

Figure 2. Design parameters for a rotationally symmetric feed-point lens.

section of an ellipse of revolution, characterized by major semi-axis, a, and focal distance, d, with center at $-\ell_1 + \ell_2 + d$. The lens-air interface is a quartic surface of revolution characterized by the distances from the intersection of that surface with the z-axis, $z = \ell_2$, to the focus of the quartic surface, $z = 0$, and to the focus of the ellipsoidal surface, $z = -\ell_1 + \ell_2$. In terms of these parameters, the quartic surface is formed by revolution about the z-axis of the locus of points given by [5, equation (2.1)]

$$\sqrt{\varepsilon_{r2}}\left(-\ell_1 + \sqrt{\Psi^2 + (\ell_1 - \ell_2 + z)^2}\right) = -\ell_2 + \sqrt{\Psi^2 + z^2} \tag{2.1}$$

where $\varepsilon_{r2} = \varepsilon_2/\varepsilon_3$, and in this case (output in air), $\varepsilon_3 = 1.0$.

The results of the lens design calculations are summarized in the following diagram, which shows a cross section of the lens through the symmetry axis. In the final design, the shape of the center conductor was modified to improve the impedance within the lens region. The

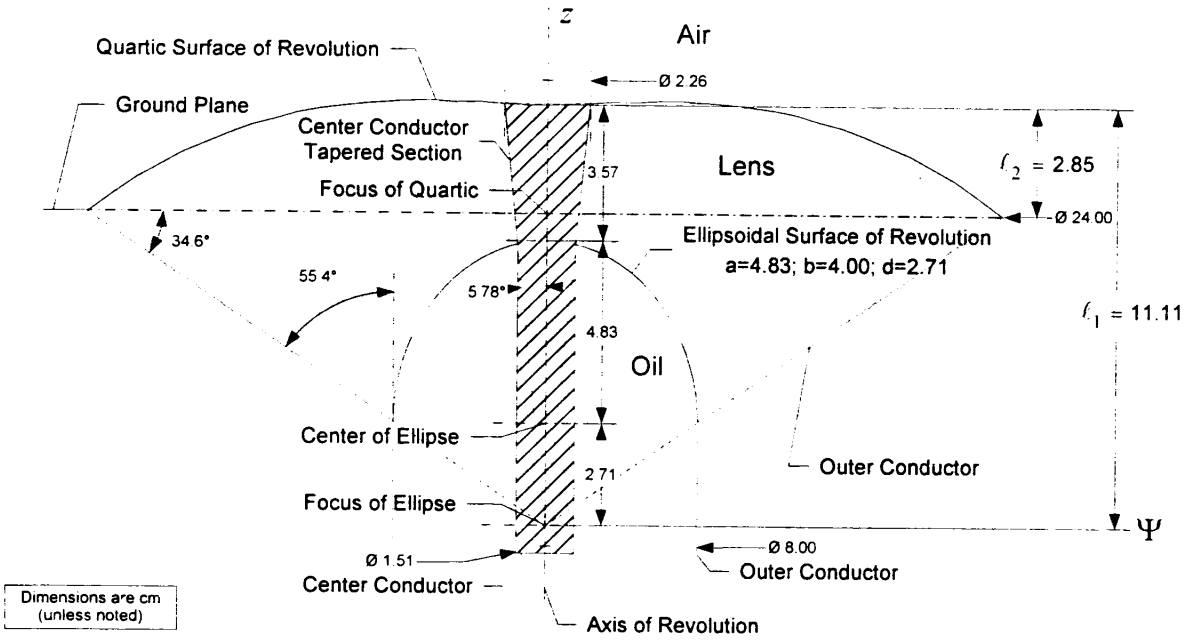

Figure 3. HIRA feed-point lens design. The relative dielectric constant of the lens is 7.0; that of the oil is 2.2.

revised section of the center conductor is shown below, in Figure 4. The reduced diameter of the center conductor was intended to ameliorate an impedance drop within the lens region. Such a drop was predicted theoretically and demonstrated experimentally with a scale-model HIRA in [7].

The figure on the next page shows the top-level assembly drawings for the HIRA which incorporated the lens designed above. Also shown are photographs of the completed HIRA as fielded for testing.

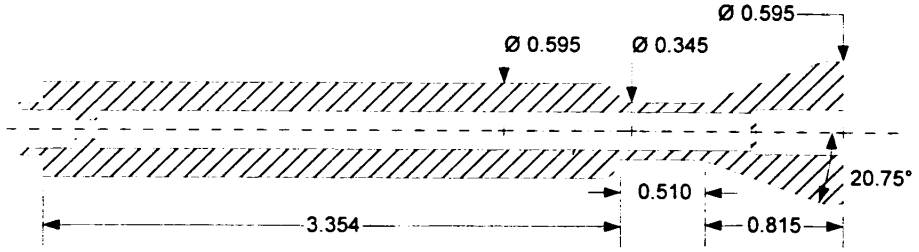

Figure 4. Modified center conductor with reduced diameter within the section embedded in the lens. (Dimensions are inches.)

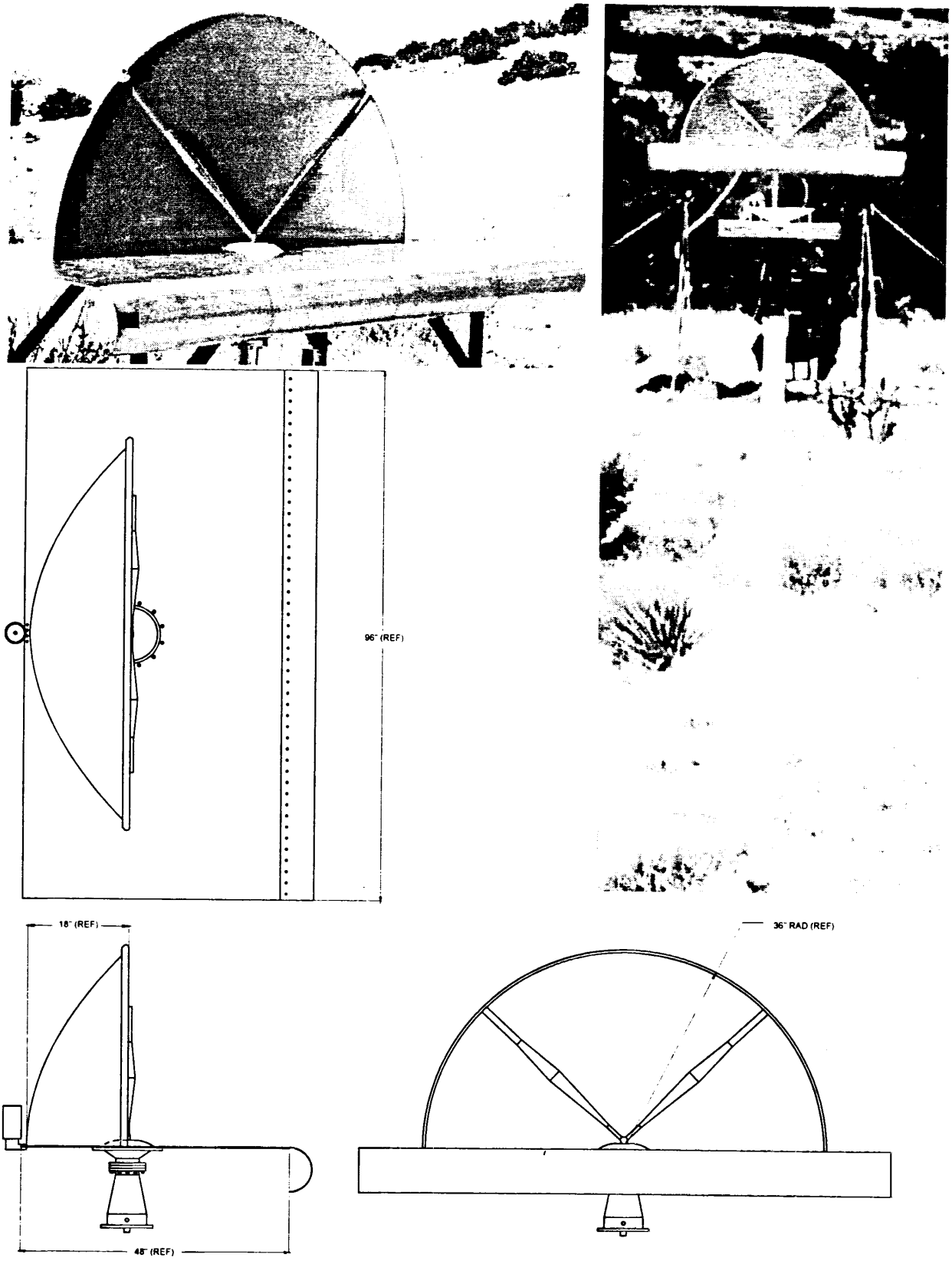

Figure 5. HIRA design and hardware.

In the preceding figure, the interface shown below the ground plane in the drawings is not the one which was built. The interface in the drawings was designed for connecting the HIRA to the output of the H-5 pulser. Subsequently, Figure 7 presents photographs of the parts of the HIRA that are located below the ground plane, specifically, of the interface to the pulser, of the oil-filled coaxial input line, and of the ellipsoidal surface of the lens.

Note also, that the feed arm design is somewhat more simple than that depicted earlier in Figure 1. In the final design, the feed arms project outward from a point above the surface of the lens, rather than from the common foci of the parabolic reflector and quartic lens surface on the ground plane at the axis of the lens. As a result, all sections of each feed arm share a common axis. This compromise in design accuracy made the feed arms considerably easier to build. Each arm was made by turning a single piece of stock on a lathe. The following figure shows the feed arm detail. The design is similar to that used in the scale-model HIRA, as reported in [7]. As

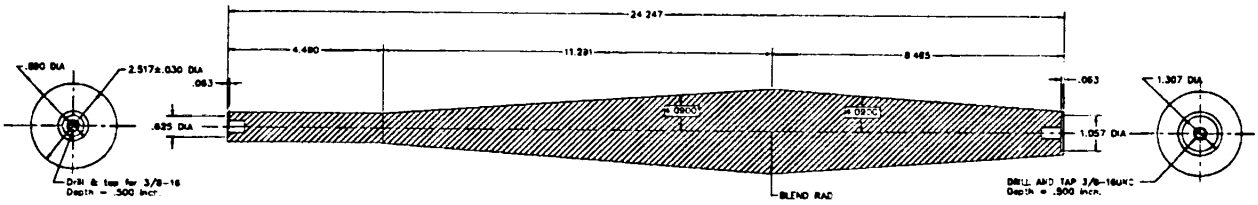

Figure 6. Feed arm section details.

explained there, the taper reversal helps to keep the impedance from sagging as the arm nears the grounded surface of the reflector. The most notable difference from the scale-model design is the cylindrical section at the lens end, where the feed arm connects to the "Y" that joins it to the other feed arm and to the end of the center conductor. This approach helps to keep the conductor radii large enough to ensure mechanical stability.

Figure 8 shows close-up photographs of both the full-scale and scale-model HIRAs. The differences and similarities in feed arm geometry are readily apparent. Note that in both HIRAs, each feed arm is resistively terminated in a matched load. In the full-scale HIRA, each feed arm is terminated at the reflector through a 200 Ω network of resistors.[†] Two parallel strings of four 100 Ω resistors in series comprise each terminator.

We turn now to presentation and discussion of the field testing of the full-scale HIRA.

[†] Low-inductance, counter-wound, wire-wound, Dale NS-10 resistors were used. As these are still too inductive at high frequencies (note the late time open circuit behavior in Figure 10), other resistor types, such as low-inductance bulk ceramics, should be considered for future designs.

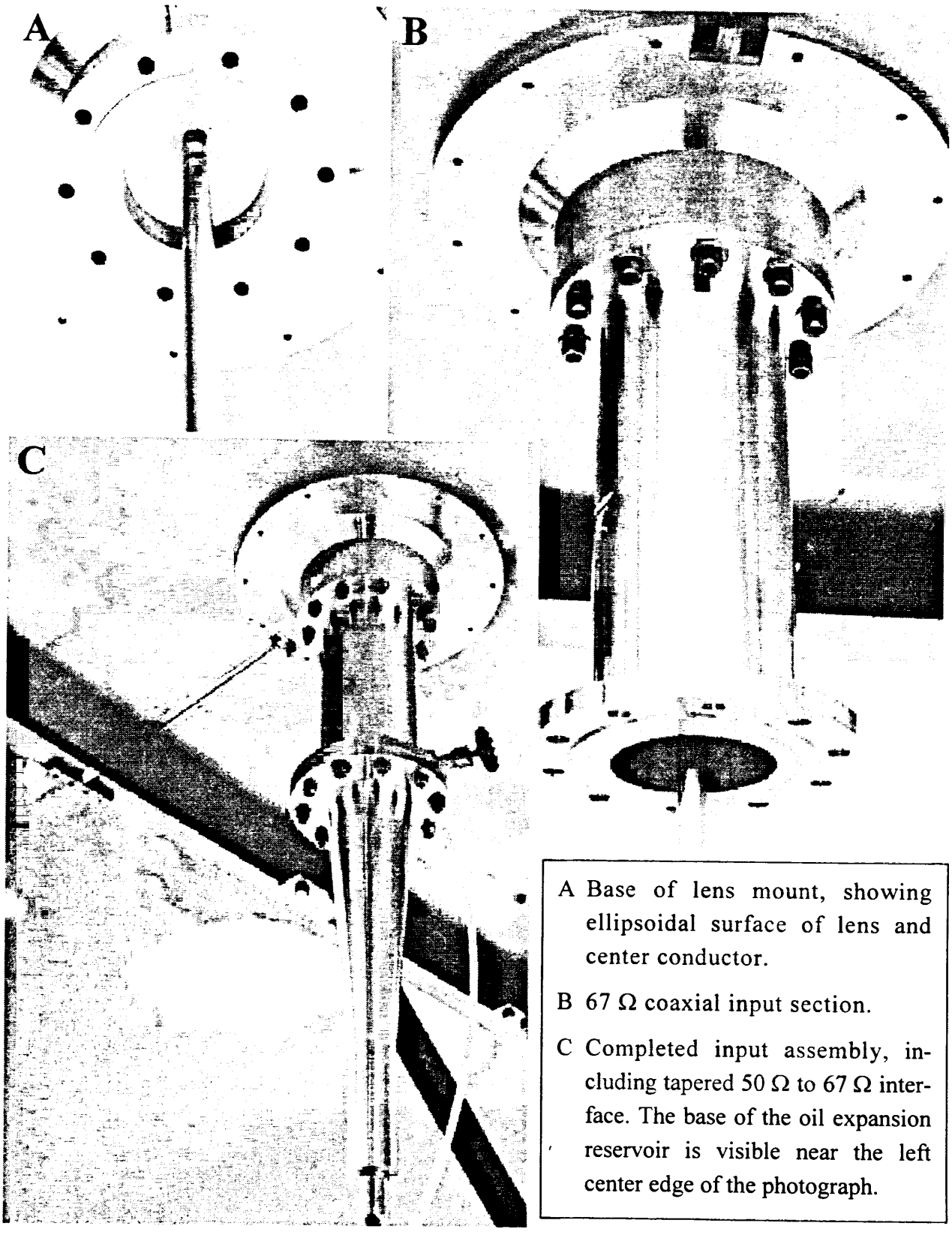

Figure 7. HIRA components located below the ground plane.

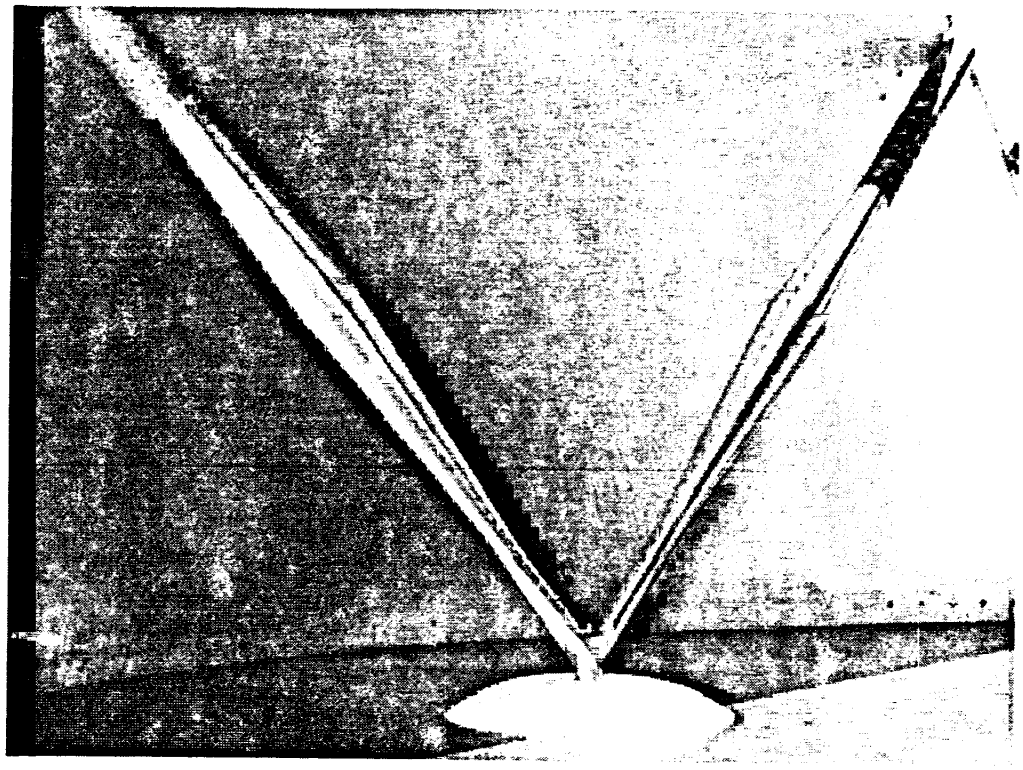

A. Full Scale HIRA

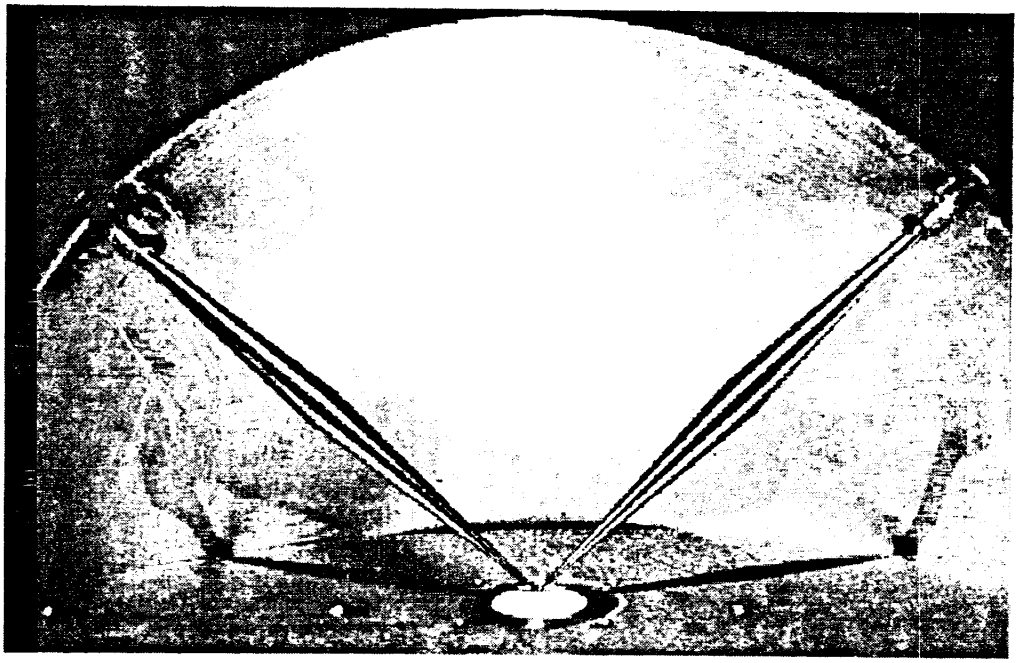

B. Scale-Model HIRA

Figure 8. Photographs of HIRA feed arm details.

3. HIRA Testing

The HIRA was assembled for outdoor testing in a remote area northwest of the Air Force Research Laboratory's HERTF on Kirtland AFB. Test equipment included a modified Picosecond Pulse Labs Model 4600 step generator, which produces a 21 V step at 50 Ω, a Tektronix 11801B digital sampling oscilloscope with SD24 sampling/TDR head and 2 m extender cable, and a prototype of the standard Farr Research 50 Ω replicating TEM sensor (Figure 9). Also available were interconnecting RF signal cables, trigger cable, and calibrated

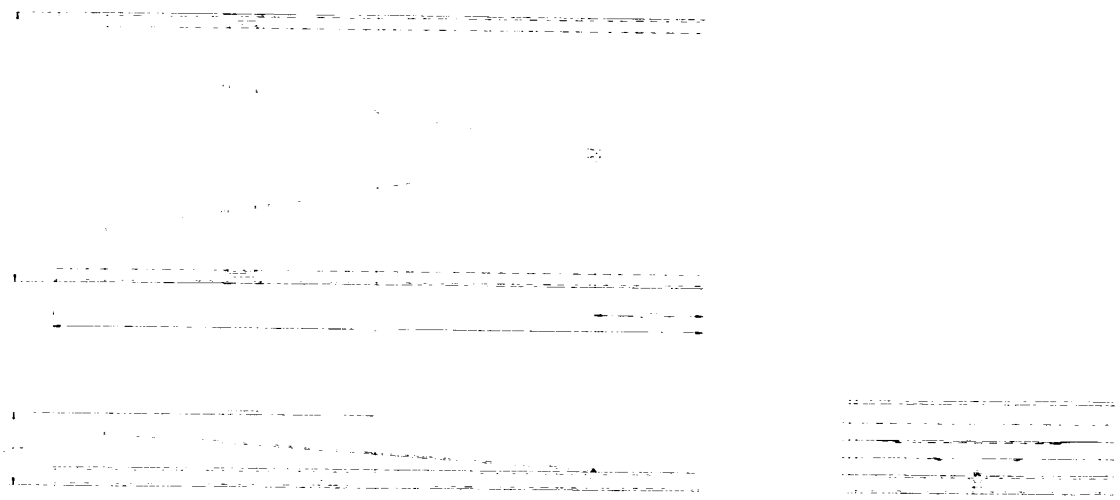

Figure 9. Replicating 50 Ω TEM sensor. (Dimensions are inches. The original prototype is shown here. We actually used a later version, in which Teflon® posts were used in place of foam to support the conducting strip.)

high-voltage RF attenuators. A portable generator supplied power for the test equipment. A 9X telescopic sight with an aluminum channel mount was used as an aid to antenna and sensor alignment.

3.1 Impedance Measurement

The impedance of the HIRA system was measured with the Tektronix 11801B by driving the antenna through a 2 ft semi-rigid coax with the 30 ps step pulse of the SD24 sampling head. The resulting TDR is shown below in Figure 10, along with annotations identifying the parts of the system responsible for the observed features. The lens assembly accounts for a relatively brief but large impedance discontinuity. Although this HIRA TDR profile closely parallels that of the scale-model HIRA shown in [7, Figure 5-4], there are several differences. For example, the larger size of the HIRA permits the SD24 TDR pulse to better resolve impedance

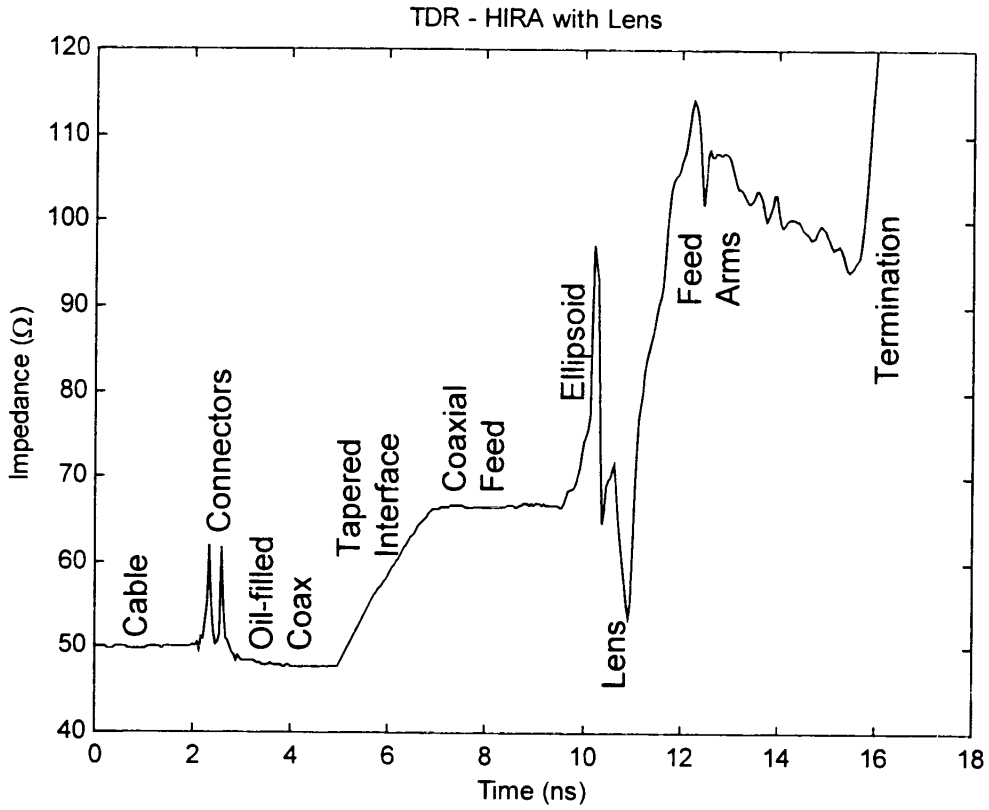

Figure 10. Impedance of the HIRA assembly.

fluctuations. Also, there is a shoulder on the rising portion of the profile corresponding to the exit from the lens; and the impedance rises to 115 Ω before declining. This behavior may be caused by a combination of the "Y" connector for the feed arms and the cylindrical sections at the base of each feed arm. Beyond the arms, the impedance rises sharply, as the somewhat inductive termination is encountered.

3.2 Radiated Electric Field Measurements

3.2.1 Test Site Configuration

Figure 11 depicts the arrangement of the HIRA and TEM sensor for radiated electric field measurements. The ground at the test site was packed dry soil with typical desert vegetation (Figure 5). The surface was mostly flat, with a slight uphill grade from the HIRA to the sensor locations. The HIRA ground plane was mounted on an adjustable Unistrut® frame at a height of approximately 2.78 m. The sensor was mounted on a tripod with extended elevator section at a height of 2.43 m. The frame holding the HIRA was tipped so that the boresight would run

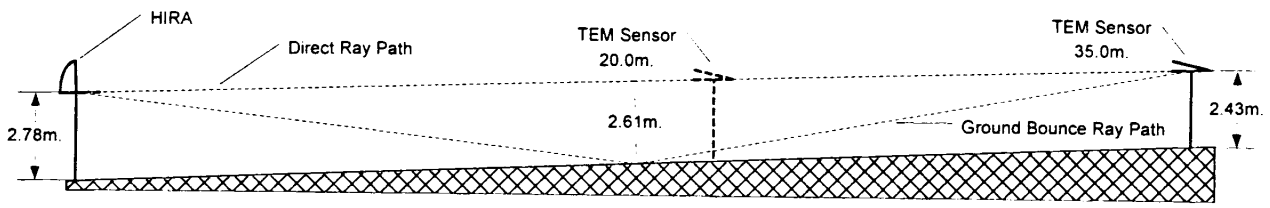

Figure 11. Physical layout of HIRA and TEM sensor for radiated field measurements. The time-of-flight for the ground bounce path is 1.3 ns longer than the direct path when the sensor is 35 m from the HIRA; it is 2.2 ns longer when the sensor is at 20 m.

approximately parallel to the ground surface. A 9X telescopic sight mounted on the HIRA ground plane was used in adjusting the sensor to a position directly on boresight. Then, the telescopic sight was moved to the sensor ground plane and used to align the sensor with the boresight direction.

3.2.2 Test Equipment Configuration

The experimental test configuration for the HIRA measurements is shown below. The Picosecond Pulse Labs 4600 step generator drives the HIRA through a type SMA connector

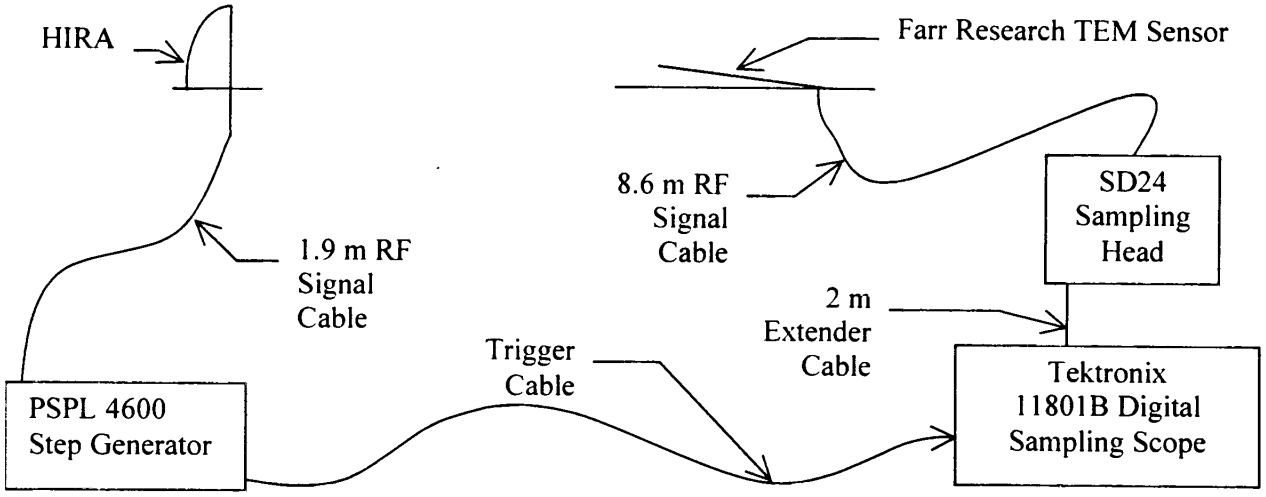

Figure 12. Experimental test setup for measuring HIRA radiation characteristics.

mounted at the base of the oil-filled input section (Figure 7C). The length of the interconnecting cable was 1.9 m. On the receive end, the Farr Research TEM sensor receives the signal, which is then passed through the 8.6 m signal cable and sampled by the SD24 sampling head and the Tektronix 11801B digital sampling oscilloscope. Data is stored in the NVRAM of the

oscilloscope and subsequently downloaded to a computer for processing by way of a GPIB connection. The signal to trigger the 11801B was supplied by the step generator. The rather long signal cable on the receive end provided additional delay to permit the 11801B to synchronize reliably with the step generator.

The TEM sensor was calibrated previously, as described in [9]. Its impulse response is shown below in Figure 13. The step generator output and its derivative, as seen through the 10.5 m total of the signal cable lengths, are shown in Figure 14. The long cables lead to a 5% attenuation of the step height to 19.5 V, and nearly double the FWHM of the derivative from 75 ps to 140 ps. The derivative is also non-gaussian. These cable effects have no significant impact on determination of the HIRA step response, however, as both the source and the sensor response are deconvolved from the raw data during signal processing.

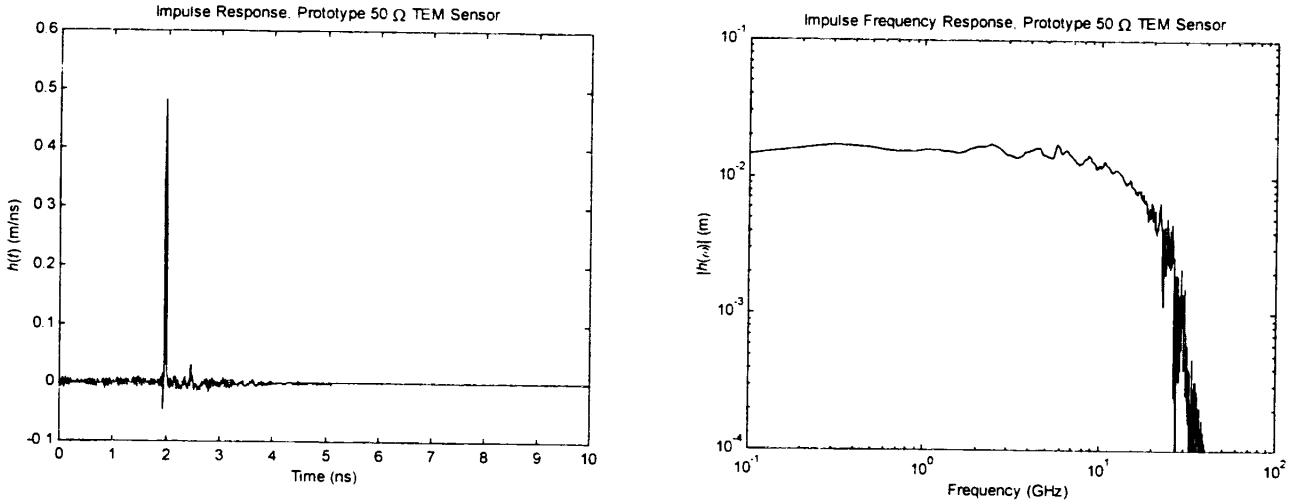

Figure 13. TEM sensor response in time and frequency domains.

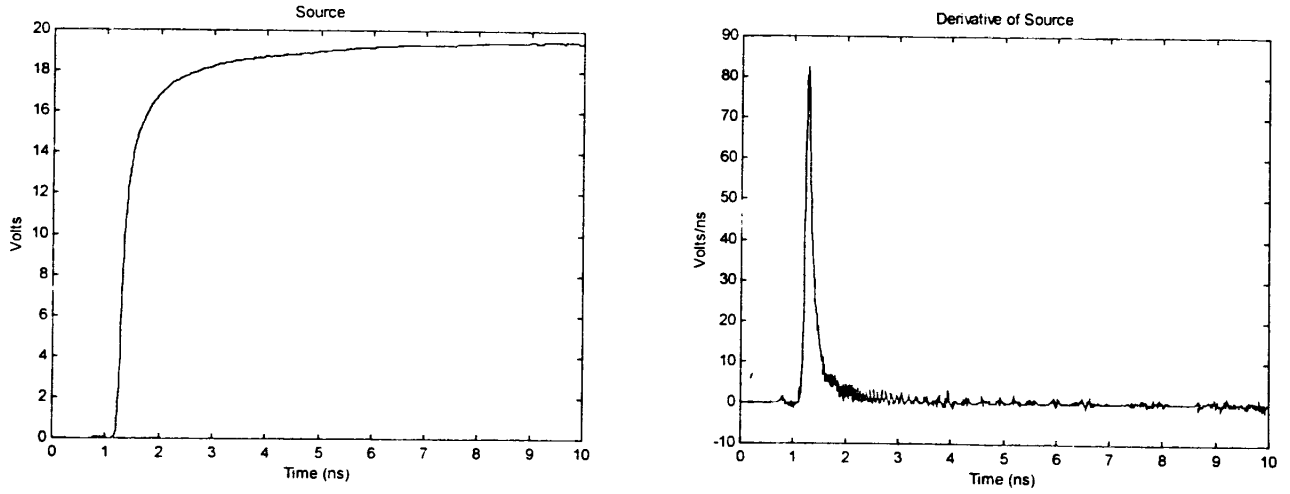

Figure 14. Voltage step and its derivative, through a 10.5 m length of RF signal cable. The maximum height of the step is 19.5 V. The FWHM of the derivative is about 140 ps.

3.2.3 Signal Processing

The voltage waveform as received by the SD24 sampling head contains contributions from the sensor impulse response, the HIRA step response, and the driving step function source. From [10] we know that the received voltage can be represented as the convolution of the sensor impulse response with the incident electric field, as

$$V^{rec}(r,t) = \tau_{SENSOR} h_{SENSOR}(t) \circ E^{inc}(r,t) \tag{3.1}$$

where τ_{SENSOR} is the transmission coefficient from the impedance of the sensor (50 Ω in our case) to the 50 Ω impedance of the cable at the output of the sensor (so that $\tau_{SENSOR} = 1.0$).

Similarly, the field radiated to a distance, r, from the aperture plane of the HIRA is related to the convolution of the antenna step response with the derivative of the source voltage at the feed arms of the reflector, as

$$E^{rad}(r,t) = \frac{1}{(2\pi c f_g r)} h_{HIRA}(t) \circ \frac{dV^{arms}(t)}{dt} \tag{3.2}$$

where f_g is the normalized impedance of the antenna, Z_{HIRA}/Z_o, and the driving function at the feed arms is related to the drive at the feed cable of the source by

$$\frac{dV^{arms}(t)}{dt} = \tau_{HIRA} \frac{dV^{src}(t)}{dt} \tag{3.3}$$

where τ_{HIRA} is the transmission coefficient from the 50 Ω feed cable impedance to the 100 Ω impedance of the HIRA feed arms.

Since a convolution with an impulse-like function can be approximated by a multiplication by the area under the impulse, we can define an effective aperture height by

$$\begin{aligned} E^{rad}(r,t) &\approx \frac{\tau_{HIRA}\, h_{eff}}{(2\pi c f_g r)} \cdot \frac{dV^{src}(t)}{dt} \\ h_{eff} &= \int_{\text{Impulse}} h_{HIRA}(t)dt \end{aligned} \tag{3.4}$$

From symmetry arguments, the integral in (3.4) is also one half of the dipole moment of the HIRA, or $a/(2\sqrt{2})$, where a is the radius of the reflector. This can be used to predict HIRA performance.

Now, by equating the radiated field in (3.2) to the incident field in (3.1), and using (3.3), we obtain

$$V^{rec}(r,t) = \frac{\tau_{SENSOR}\tau_{HIRA}}{(2\pi c f_g r)} h_{SENSOR}(t) \circ h_{HIRA}(t) \circ \frac{dV^{src}(t)}{dt} \tag{3.5}$$

Thus, by deconvolving the sensor response from the received voltage, we can obtain a measure of the radiated electric field at the sensor location. Furthermore, by deconvolving both the sensor response and the source derivative from the received voltage, we can obtain the HIRA step response.

3.2.4 Test Protocol and Data Analysis

Measurements of the electric field radiated by the HIRA were made on boresight at distances of both 35 and 20 meters from the focus of the reflector, as indicated previously in Figure 11. Data were also obtained at representative offsets from boresight. Signal processing generally employed the techniques of [11, Section III], and followed the approach outlined above.

On the top left in Figure 15, is the raw waveform observed on boresight at 35 m. The primary HIRA response is the impulse at 4.2 ns, with a FWHM of 216 ps. The inverted peak beginning at about 5.5 ns is ground bounce. On the top right, is the raw waveform after time-gating out the ground bounce. The bottom two graphs compare the corresponding frequency domain step responses. Note the absorption bands which are contributed by the radiation reflected from the ground when ground bounce is retained. We routinely time-gated out ground bounce and later contributions to the received waveforms prior to any other signal processing.

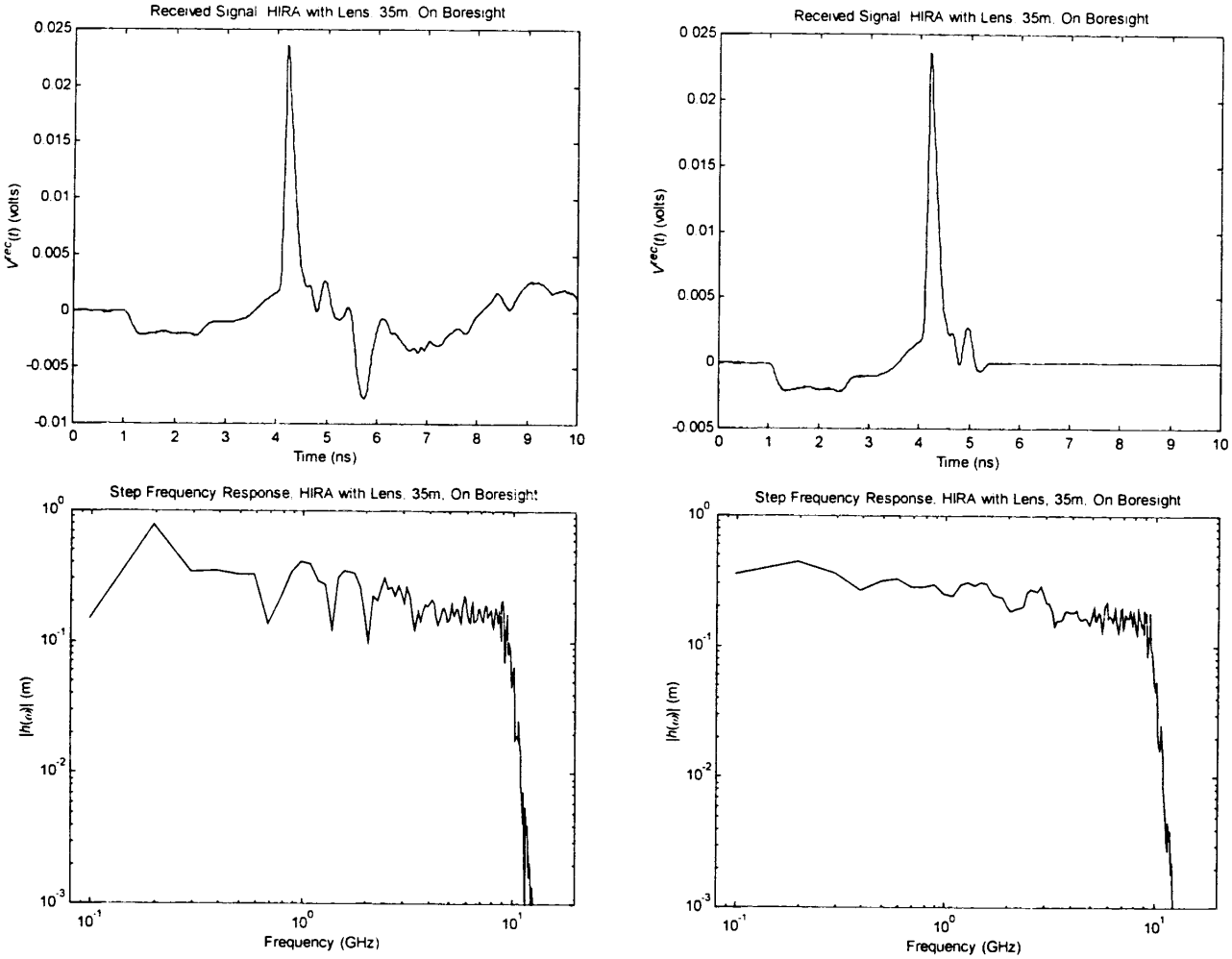

Figure 15. Impact of ground bounce. The top two graphs show raw received signal before (left) and after (right) removal of the ground bounce peak. The bottom two graphs show the corresponding frequency domain step responses. Note the soil absorption bands in the left graph, where ground bounce is retained.

To process the raw test data, we first establish the values of the time-independent parameters appearing in equations (3.1) through (3.5). Since the impedance of the sensor and of the cable to the SD24 sampling head were both 50 Ω, the voltage transmitted to the sampling head is the same as that received at the sensor aperture. Thus, $\tau_{SENSOR} = 1.0$. In contrast, we saw in Figure 10 that both the step generator output and feed cable impedance were 50 Ω, while the HIRA feed arm impedance was approximately 100 Ω. We assume an abrupt impedance transition and write

$$\tau_{HIRA} = \frac{2Z_{HIRA}}{Z_{HIRA} + Z_{PULSER}} \tag{3.6}$$

finding $\tau_{HIRA} = 1.33$. Also, since $Z_{HIRA} = 100\ \Omega$, we have $f_g = 0.2654$.

In presenting the radiated field obtained by deconvolving the sensor response from the received voltage, it is convenient to introduce normalized units. Thus, instead of graphing $E^{rad}(r,t)$ and, in the frequency domain, $E^{rad}(r,\omega)$, we present the corresponding values of rE^{rad}/V_o, where V_o is a reference voltage. In the far-field,‡ this normalized function is independent of the range, r. In the time domain, it is dimensionless; in the frequency domain, its units are 1/GHz. For the reference voltage, we choose the maximum of the voltage step applied at the feed arms. From Figure 14, the maximum voltage at the HIRA input, $V_{\max}^{src}$, is 19.5 V. Thus, from $V_o = \tau_{HIRA}\, V_{\max}^{src}$, we obtain 25.9 V at the feed arms.

The normalized radiated field data are presented in Figure 16. The impulse maxima are approximately equal for both 35 m and 20 m ranges, as we would expect for far-field measurements. The magnitude, 2.0, is about half the predicted value for our driving source [12, equation (5.1), *et seq.*]. Although boresight alignment error and reflection losses may contribute to this difference, the primary cause is probably the compromise we made in design of the feed point. Recall that there is a minor offset between the apparent intersection of the feed arms and the focus of the reflector (see Figure 8A). This leads to some broadening of the impulse, thus reducing its maximum.

Next, the data are processed to extract $h_{HIRA}(t)$, the HIRA response to a step input. These step response results are presented in Figure 17. On boresight, we see an impulse with a FWHM of about 70 ps and maximum in the 3.2 to 3.8 m/ns range. As with the normalized fields, the on-boresight step response should be independent of range. Finally, in Figure 18, we provide the integral of this impulse. From (3.4), the jump in the integral of $h_{HIRA}(t)$ gives us the effective

‡ Specification of what constitutes the far-field for an impulse field is open to some discussion. As a working definition, we assume that a range greater than $3a^2/2ct_r$, where a is the reflector radius, is in the far-field. For a gaussian impulse, the rise time is about 1.09 times the FWHM [12]. The FWHM of our source is about 140 ps, leading to a far-field range of 27 m. The FWHM of the radiated impulse is at least 212 ps, corresponding to a far-field range of only 18 m. On the basis of these observations, it appears safe to conclude that our 20 m measurement location was at the near edge of the far-field, while the 35 m measurements were clearly within the far-field.

aperture height of the HIRA, h_{eff}. On boresight, we obtain approximately 0.36 m. Since the reflector radius is 0.9144 m (36 inches), we expect to see $0.9144/(2\sqrt{2}) = 0.32$ m. Thus, our h_{eff} is only about 11% higher than expected; and we conclude that our measurement is consistent with theory.

The following table summarizes the results of the HIRA measurements.

Range (meters)	Position Relative to Boresight		Radiated Field (Normalized)		Step Response		Effective Aperture Height (meters)
	Distance (meters)	Angle (degrees)	Peak	FWHM (ps)	Peak (m/ns)	FWHM (ps)	
35.	0.	0.	2.00	212.	3.76	70.	0.359
	0.6	1.	1.86	230.	2.94	84.	0.363
	1.2	2.	1.60	275	1.84	170.	0.356
20.	0.	0.	1.87	222.	3.22	76.	0.352
	1.6	5.	1.03	482.	0.88	300.	0.349

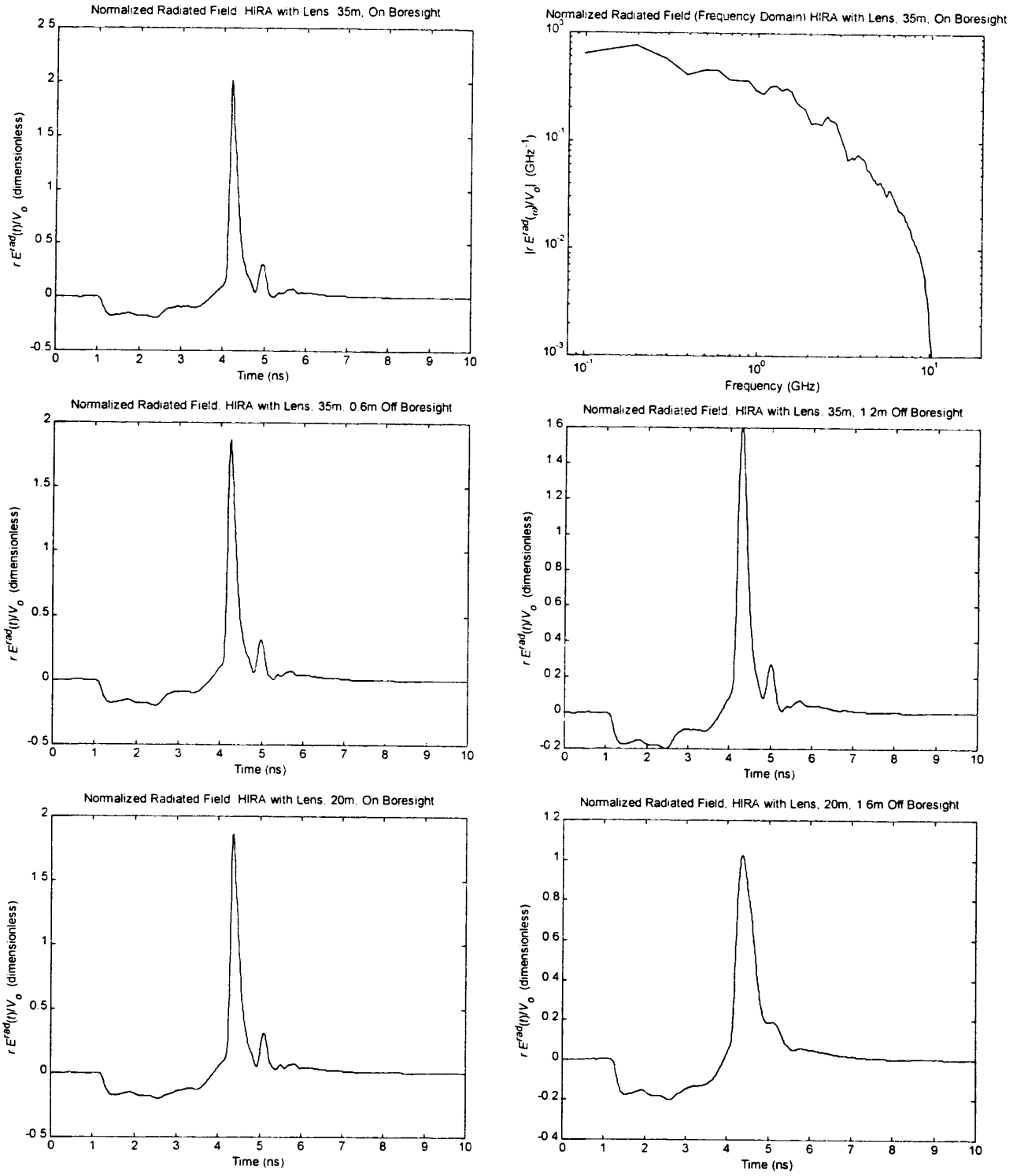

Figure 16. Normalized radiated electric fields at 35 and 20 meter ranges, both on and off boresight. The reference voltage, V_o, is 25.9 volts.

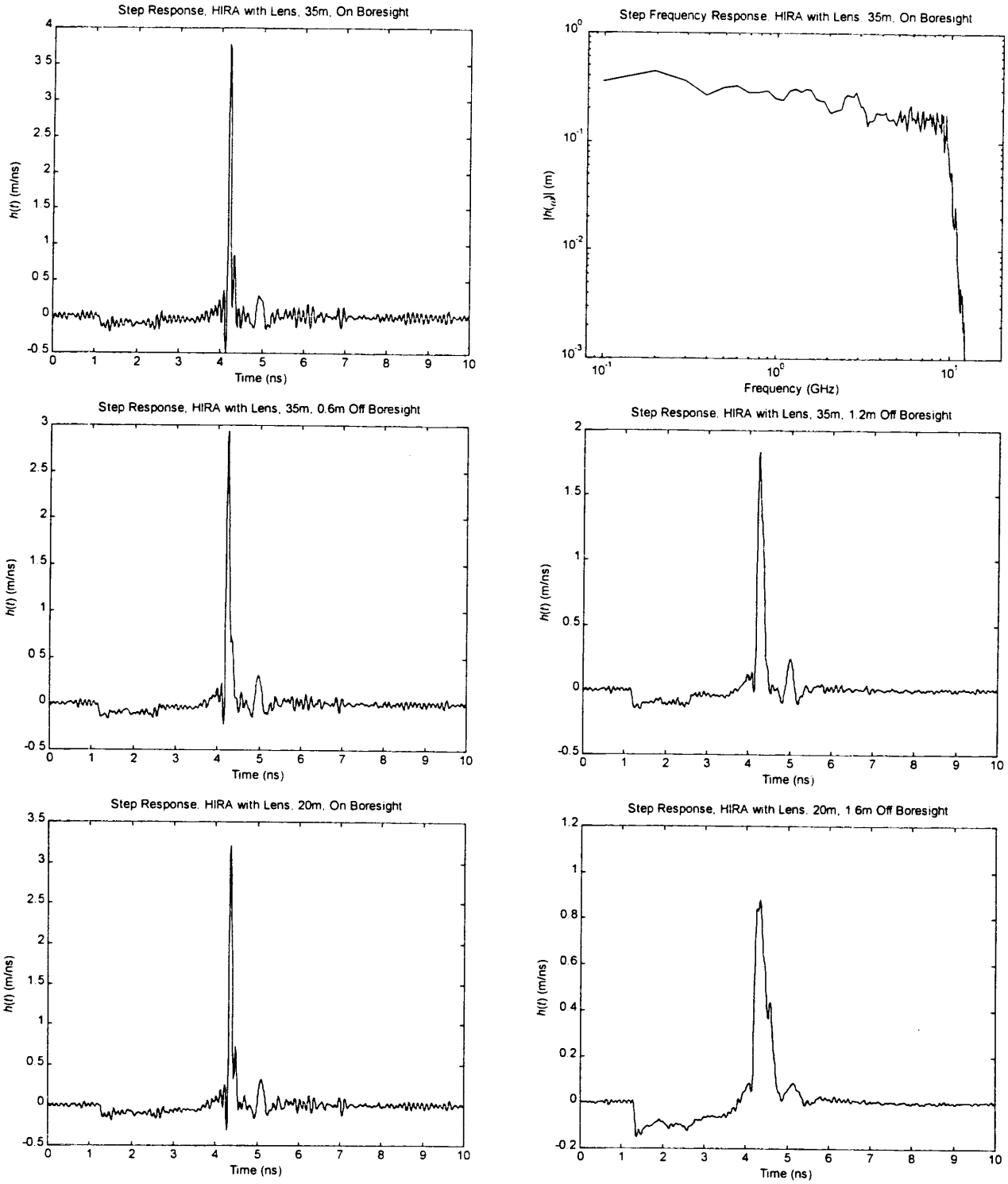

Figure 17. Step response of the HIRA, as observed from 35 and 20 meter ranges, both on and off boresight.

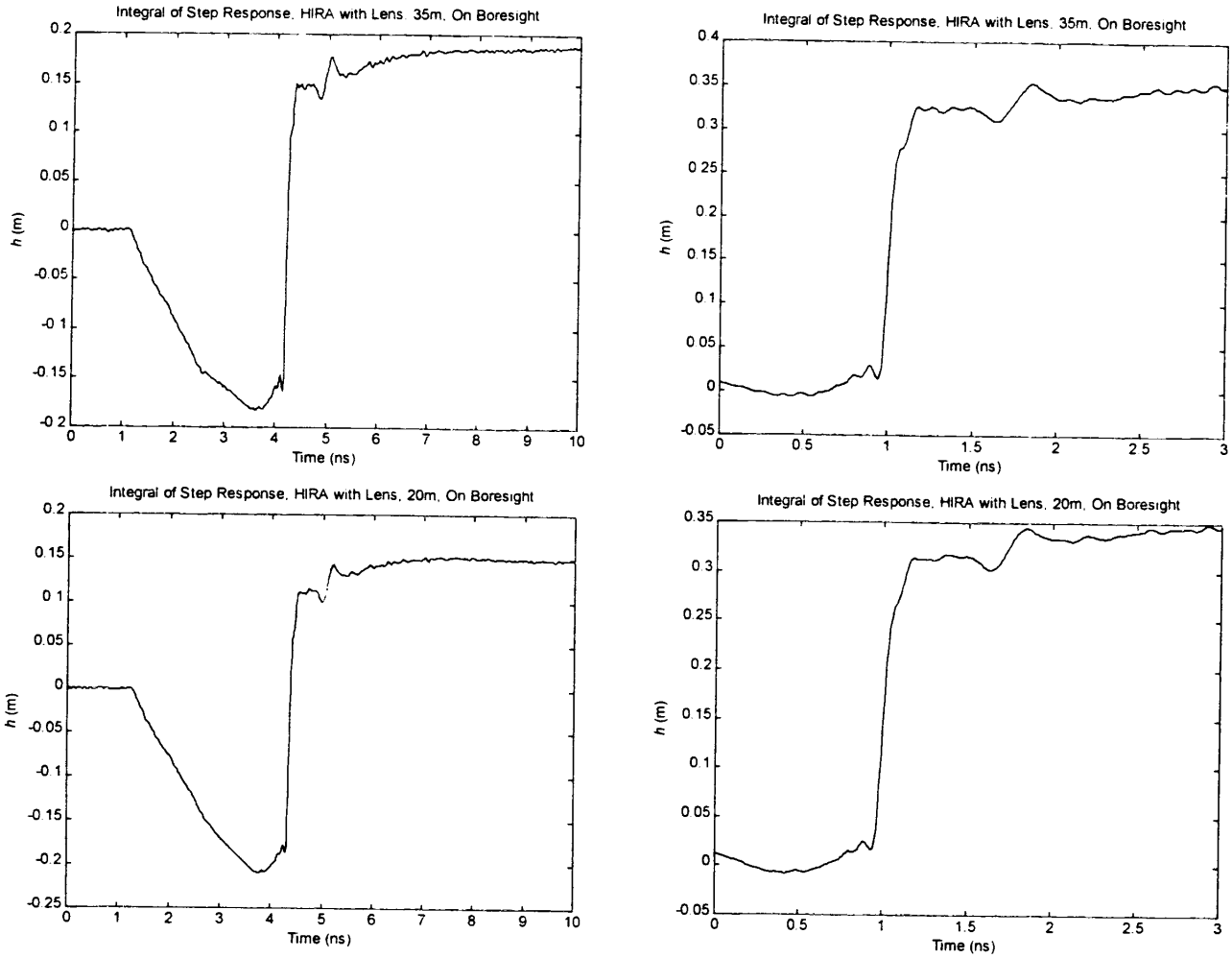

Figure 18. Integral of HIRA step response, as observed at 35 and 20 m ranges, on boresight. The jump in the integral is the effective aperture height. It is the area under impulse of $h_{HIRA}(t)$.

4. Conclusions

The measured effective aperture height of the antenna is approximately 11% greater than the theoretical value. The antenna step response is an impulse with a FWHM on boresight of 70 ps. As a result of impulse broadening arising from compromises in the feed-point design, the peak electric field radiated on boresight is reduced. This has no effect, however, on the area under the impulse. We conclude that the antenna performance is consistent with both theory and design.

Acknowledgments

We would like to thank Dr. Carl E. Baum, of the Air Force Research Laboratory, for many insightful discussions that contributed to this effort. We would also like to thank Mr. William D. Prather, also of the Air Force Research Laboratory, for arranging funding for this work.

References

1. C. E. Baum, *Variations on the Impulse-Radiating Antenna Theme*, Sensor and Simulation Note 378, February 1995.

2. E. G. Farr and C. E. Baum, *Impulse Radiating Antennas with Two Reflecting or Refracting Surfaces*, Sensor and Simulation Note 379, May 1995.

3. C. E. Baum and A. P. Stone, *Transient Lens Synthesis: Differential Geometry in Electromagnetic Theory*, Appendix I, Taylor and Francis, New York, 1991.

4. E. G. Farr and C. E. Baum, *Feed-Point Lenses for Half Reflector IRAs*, Sensor And Simulation Note 385, November 1995.

5. W. S. Bigelow, E. G. Farr, and G. D. Sower, *Design Optimization of Feed-Point Lenses for Half Reflector IRAs*, Sensor and Simulation Note 400, August 1996.

6. W. S. Bigelow and E. G. Farr, *Design of a Feed-Point Lens with Offset Inner Conductor for a Half Reflector IRA with F/D Greater than 0.25*, Sensor and Simulation Note 410, September 1997.

7. G. D. Sower, L. M. Atchley, D. E. Ellibee, W. S. Bigelow, and E. G. Farr, *Design for Half Impulse Radiating Antennas: Lens Material Selection and Scale-Model Testing*, Measurement Note 54, February 1998.

8. E. G. Farr, G. D. Sower, and C. J. Buchenauer, *Design Considerations for Ultra-Wideband, High-Voltage Baluns*, Sensor and Simulation Note 371, October 1994.

9. E. G. Farr, C. E. Baum, and W. D. Prather, *Multifunction Impulse Radiating Antennas: Theory and Experiment*, Sensor and Simulation Note 413, November 1997.

10. E. G. Farr, E. E. Baum, and C. J. Buchenauer, "Impulse Radiating Antennas, Part II," p. 159-170, in *Ultra-Wideband, Short-Pulse Electromagnetics 2*, New York, Plenum Press, 1995.

11. E. G. Farr and C. A. Frost, *Compact Ultra-Short Pulse Fuzing Antenna Design and Measurements*, Sensor and Simulation Note 380, June 1995.

12. E. G. Farr and G. D. Sower, *Design Principles of Half Impulse Radiating Antennas*, Sensor and Simulation Note 390, December 1995.